Microstructure Effects on Fatigue Crack Growth in Additively Manufactured Ti-6Al-4V

Raeann VanSickle, David Foehring, Huck Beng Chew, John Lambros*

Department of Aerospace Engineering, University of Illinois at Urbana-Champaign, Urbana IL 61801, USA

*Author to whom all correspondence should be addressed. Email: lambros@illinois.edu

Abstract

In this work we investigate the relationship between the different microstructural features in additively-manufactured (AM) Direct Metal Laser Deposited Ti-6Al-4V alloys and the observed fatigue and fracture behaviors, using high resolution Digital Image Correlation experiments and microstructural imaging. Fatigue cracks in the AM specimens were observed to periodically propagate parallel to the α' laths and deflect at prior β grain boundaries. Corresponding plastic strain distributions show needle-like regions of high strain that correlated to the α' laths, suggesting significant influence of the microstructure on the plastic zone. In many cases, the fatigue cracks also propagated towards voids from unsintered powder or gas entrapment in the vicinity. In several experiments, premature failure of the AM specimens occurred under monotonic fracture or cyclic fatigue loading, which we attribute to the presence of void clusters located near the crack-tip. These fatigue and fracture characteristics were similar for AM specimens of different build-orientations.

Keywords: Additive manufacturing; fracture; fatigue; defects; microstructure; plastic wake

1. Introduction

Additive manufacturing (AM) of metals is revolutionizing the aerospace industry with the ability to create complex part geometries and to consolidate many part components into one, thus reducing component weight, material waste, and assembly complexity. Compared to traditional subtractive manufacturing methods, AM processing allows for shortened lead time on parts by moving production in house [1,2], which can enable the on-demand creation of spare parts in situations not easily accessible to a supply chain (e.g., in vessels at sea or in space) [3]. In addition, AM has become a valuable tool in obtaining spare parts for structures that are no longer in production [4]. One common type of AM alloy widely used for aircraft structural components is Ti-6Al-4V, which exhibits high strength, low density, high fracture toughness, and excellent corrosion properties. Conventional manufacturing of Ti-6Al-4V involves extrusion, forging, casting, and secondary machining processes to achieve the desired shapes, all of which can be extremely challenging given the propensity of the alloy to strain harden. In contrast, AM processes are capable of producing near-net shape structures of complex geometries directly from three-dimensional CAD models by adding material incrementally.

One of the more common AM techniques used to fabricate Ti-6Al-4V is powder bed fusion using Direct Metal Laser Melting (DMLM). In DMLM, Ti-6Al-4V powder particles are distributed in a thin layer over a build plate. The first powder layer is completely melted by a laser, before a new layer of powder is distributed over the preceding layer, and the process is repeated in succession, thereby adding material until the build is complete [5]. The highly concentrated laser energy source generates high temperatures of ~2600K in the melt pool [1], which transforms the initial $\alpha+\beta$ phase of the Ti-6Al-4V powder into a pure β phase. Because of the short interaction time, high cooling rates of 10^4-10^6 K/s are also generated [1]. Once the Ti-

6Al-4V layer cools past its β transus temperature of 995°C [6], the β phase now transforms into martensitic α' phase that nucleates within these β grain boundaries, resulting in observable "prior β grains" [7,8] which tend to form in a columnar shape along the build direction and span the length of many build layers [1,9]. A thin layer of coarsened microstructure is observed periodically, perpendicular to the build direction, and is attributed to the re-melting of layers [1,10]. This coarsened microstructure creates a banded type structure that is sometimes referred to as a "layer band" [1,9-12].

The mechanical behavior of AM Ti-6Al-4V depends not only on any post processing of the material (such as surface finishing or heat treatment), but more importantly on the initial parameters used in the build process (such as laser power and scan speed) as these influence the amount and type of defects within the material. Common defects in AM Ti-6Al-4V include gas entrapment voids (or pores), lack-of-fusion pores, and un-melted powder particles on the as-built surface. Gas entrapment voids are usually spherical and occur when gas becomes trapped in the melted Ti-6Al-4V during the laser melting process, while lack-of-fusion defects are typically irregular in shape and sometimes form due to inadequate laser energy that results in incomplete melting [1]. As a result, there are varying reports regarding the fracture toughness and fatigue life of AM Ti-6Al-4V. Many studies indicate as-built DMLM Ti-6Al-4V samples exhibit lower fracture toughness in comparison to wrought Ti-6Al-4V and attribute this reduction in fracture toughness to the martensitic microstructure [13-17]. However, the fracture toughness is also shown to exceed the wrought value in several studies when the additive material is heat-treated [13,16]. Some studies suggest that a difference in fracture toughness could be attributed to the sample build orientation [15,17]. This anisotropic behavior has also been observed in high cycle fatigue tests of DMLM [18]. The fatigue life of DMLM Ti-6Al-4V samples has been reported to

be lower than wrought Ti-6Al-4V samples [19,20]. Mower and Long attribute this reduction in fatigue life to fatigue cracks that initiate from voids on the surface and within the samples and report that fatigue life can return to 70% of the wrought values after hot isostatic pressing [19].

In this work, we investigate the relationship between the different microstructural features in AM DMLM Ti-6Al-4V alloys and the observed fatigue and fracture behaviors, using high resolution Digital Image Correlation (HiDIC) experiments and microstructural imaging. Our experiments will focus on the correlation of plastic strain accumulation, microstructural features such as prior β grain boundaries and α' laths, and location of defects such as voids and lack-of-fusion defects, with the goal of understanding how these different microstructural features and defects of AM versus conventionally manufactured Ti-6Al-4V alloys impact the fatigue crack growth mechanisms, and ultimately, the fatigue life of the metal.

2. Experimental Methods

2.1 Specimen geometry and sample preparation

Single-edge notch tension Ti-6Al-4V specimens, with dimensions as shown in Fig.1a, were additively-manufactured with DMLM to near net shape with a powder bed deposition layer thickness of 30 μm. In the DMLM process, the powdered metal is spread across the entire build platform and selectively melted to previous layers using a laser, which allows metal parts to be built out of a bed of powdered metal layer by layer. Our Ti-6Al-4V specimens were procured from GPI Prototype & Manufacturing Services and were additively-manufactured with an EOSINT M290 machine, which utilizes a 400 W Yb-fiber laser, with a scan speed of up to 7 m/s and a focus diameter of 100 μm. For the majority of the samples used here the build direction

was along the loading direction (y-axis). These samples are denoted as AM-Y#, where # represents a sample number. However, one AM sample tested (AM-Z1) was built along the thickness direction (z-axis). It was only possible to obtain one such AM-Z sample with a through-thickness build that did not possess obvious warping or initial damage. A 1 mm long edge notch at the mid-point of each sample was machined using a 0.15 mm radius electric discharge machining (EDM) wire. Two holes were drilled on the sample centerline, as shown in Fig. 1a, where pins were inserted in order to ensure sample alignment with the loading axis of the tensile machine. For comparison studies, we also fabricate conventional Ti-6Al-4V samples of the same dimensions from a 1.6 mm thick grade 5 (Ti-6Al-4V) annealed titanium sheet (procured from McMaster Carr) using EDM.

AM samples were ground on all sides and edges with 320-grit SiC paper step to remove all unsintered particles. The surface on one side of all samples (additive and conventional) was prepared for imaging using a three-step grinding process (using 320-, 600-, and 800-grit SiC paper) followed by polishing and ultrasonic cleaning. All samples were then vibratory polished for 1 to 2 hours, followed again by ultrasonic cleaning in both distilled water and either ethanol or isopropyl alcohol. Along the lines of the approach of Carroll et al. [21], after grinding and polishing, Vickers hardness indents were placed at the corners of an area of interest using a Shimadzu hardness indenter. These indents served as fiducial markers that were used to align the observed microstructure to the measured strain fields.

2.2 Fatigue experiments

A fatigue crack was grown from the starter EDM notch using an Instron 8500 mechanical test frame with a 4.45 kN load cell, as shown in Fig. 1b. Samples were cyclically loaded in load control with a haversine waveshape at a frequency of 1 Hz, with a stress intensity factor range

$\Delta K = K_{max} - K_{min} = 19.8$ MPa√m and a load ratio of $R = \frac{K_{min}}{K_{max}} = 0.1$, where K_{max} and K_{min} are the maximum and minimum mode I stress intensity factors respectively. This ΔK value is approximately one third of the published mode I critical stress intensity factor of conventional Ti-6Al-4V [22] and was selected as a compromise between the amount of plasticity present in the experiments and the time it would take to grow the fatigue crack.

Crack initiation was observed around 2,000 to 3,000 cycles for most samples. As the fatigue crack propagates, the ΔK value would increase if the load were kept constant. To avoid the resulting significant growth of strains in the plastic wake, a load shedding procedure was adopted where the load was reduced by 10% whenever ΔK exceeded the target value of 19.8 MPa√m by 5%. This load shedding procedure was repeated until we achieved a total fatigue crack length of either 2 mm or 3 mm, including the notch.

2.3 Plastic strain measurements using HiDIC

We trace the plastic strain developments during fatigue cycling with high resolution DIC (HiDIC) [21]. A microscale resolution pattern was developed by depositing silicon carbide powder particles on the sample polished surface. Images were acquired with a Point Grey Grasshopper 3 2016 x 2016 pixel resolution CCD monochromatic camera attached to an Olympus microscope. We recorded 20x magnification optical images of the expected cracking region of the samples at the initial state prior to loading. In order to cover the entire area of interest, images were taken with the microscope in a grid-like fashion, with at least a 50% overlap of each image. A stitched grid of anywhere from 30 to 84 images were used. The outer edge of each image was cropped, and the images were stitched using ImageJ [23], as described in [21], to obtain one high-resolution image. Once fatigue cracking was completed, the samples were carefully removed from the load frame and a second set of 20x images of the region of

interest were taken, stitched and correlated with the first (using a 21x21 pixel subset size and a step size of 5 pixels) in order to determine the extent of the plastic wake formed. Since these images were taken under an optical microscope after loading was removed, only residual (plastic) strains are recorded by HiDIC. The effect of image stitching on HiDIC strain fields is discussed in Carroll et al. [21] who note that artificial bands of high-low strain may appear along the boundary of images, but that this error becomes less dominant as global strain approaches 1%. In order to validate the ex situ DIC pattern two sets of images were taken, stitched and correlated, paying attention to the strain field noise generated rather than displacement noise.

2.3 Microstructural characterization

Heat tinting is a microstructural characterization technique that can be used to identify grain phase and orientation information. Heating a polished metal sample produces an oxide layer that varies in thickness based on the material phase and crystallographic orientation. This variation in oxidation layer thickness produces different colors that can be observed through polarized or brightfield microscopy. While there are a variety of ways to heat tint a sample, a laboratory oven provides a controlled environment allowing for reproducible results [24]. Heat tinting provides the best results with a flat mirror polished surface, however it still produced acceptable results with lower quality surface finishes and embedded abrasive particles from polishing, as in some cases studied here. VanderVoort [24], Harper et al. [25], and Barnes [26] all present different heat tinting procedures for commercially pure titanium and titanium alloys using different temperatures (ranging from 400°C to 700°C) and times (ranging from 30 seconds to 2 hours).

Adopting the procedure outlined by Harper et al. [25], both the conventional and the AM Ti-6Al-4V samples were placed in a laboratory furnace at 566°C and removed after 8 minutes. Microstructural images were captured with the same optical microscope system used for the

HiDIC measurements but often at a higher magnification. Figure 2a shows the heat-tinted microstructure of a conventional Ti-6Al-4V specimen at 40x magnification, which has an equiaxed α phase (grey spots; grain size of ~9.5 μm) intermixed with a β phase (dark spots), resembling the annealed conventional Ti-6Al-4V microstructure reported in prior studies [6,27-30]. In contrast, the heat-tinted AM samples with build directions along the y-axis, termed AM-Y4 and AM-Y3 in Figs. 2b and 2c, reveal a fine martensitic (α') structure (grain size of ~1 μm) with elongated columnar prior β grains (grain size of ~110 μm) along the build direction, similar to that reported in prior studies [9,13,31]. The heat-tinted AM sample with build direction along the z-axis, termed AM-Z1 in Fig. 2d, reveal a checkerboard pattern of prior β grains, as also seen in similarly-oriented DMLM samples in prior studies [31-33]. Interestingly, the AM-Y3 sample has many visible surface pores (or voids) with arrows pointing out some of the larger defects.

2.4 Layer banding

Unlike conventional Ti-6Al-4V, one unique feature of the AM material is the presence of regularly spaced dark "layer bands" oriented perpendicular to the build direction, as shown for the AM-Y1 sample in Fig. 3a. These layer bands are consistently spaced 85 μm apart for the 30 μm layer build samples, which is ~3 times the powder layer thickness. Layer bands seen in AM Ti-6Al-4V have been widely reported in the literature [10,34-41], and were attributed to the complex thermal history that AM metals undergo as layers are initially deposited, melted, and remelted and reheated by laser scanning of subsequent layers. In Thijs et al. [38] it was proposed that segregation of aluminum occurred due to the fast solidification of the melt pool, and thus Ti_3Al phase precipitates were formed in these layer bands and produced the contrast seen in optical and SEM micrographs. Fluctuations in aluminum content seen in energy dispersive x-ray spectroscopy (EDS) measurements were used to confirm this. Kelly and Kampe [36] investigated

the nature of these layers using hardness, composition fluctuations, and microstructure of laser melted Ti-6Al-4V. Hardness tests were performed in that effort on the suspicion that oxygen contamination embrittled the samples at the layer interfaces. However, no significant hardness variation between layer bands and in-between regions led to that hypothesis being ruled out. Composition analysis was used to determine any amount of atomic segregation within and between layer bands, and contrary to conclusions drawn in Thijs et al. [38], no Ti_3Al segregation was found in Kelly and Kampe [36]. Micrographs of chemically etched samples in Kelly and Kampe [36] showed Widmanstätten α phase structure in the layer bands compared to a coarser basketweave a structure in the surrounding areas. It was then concluded that the appearance of these layer bands is due to thermal heating across several layers resulting in these structural differences between layers [36].

Following Kelly and Kampe [36], we performed microhardness measurements on a polished face of an AM-Y sample with a 100 g weighted indenter to achieve an indentation size resolution necessary for hardness measurements within a layer band. The microhardness indentations are then superposed on an SEM backscattered electron composition mode image, as shown in Fig. 3b, to determine indentation locations with respect to the layers. We obtain an average Vickers hardness number (VHN) of 449.1 with standard deviation of 19.9 between the layer bands and an average VHN of 445.0 with standard deviation of 23.9 on the layer bands, indicating no significant variations in hardness, akin to previous findings [36]. We also performed a line scan composition analysis on an AM-Y sample using a JEOL 6060LV SEM, and observed no significant fluctuations in the composition of any constituent element along the build direction at layer interfaces, as shown in Fig. 3c, which again agrees with previous findings in [36].

3. Results and Discussions

3.1 Plastic strain accumulation

Under cyclic (elastic) fatigue loading within the conditions of small-scale yielding, a small (relative to large scale yielding) plastic zone will form in front of a notch or crack tip. As a fatigue crack eventually initiates and grows, a new (active) plastic zone will propagate along with the growing crack, thus leaving a wake of plastically deformed material on either side of the crack. By recording images prior to cracking and correlating these with images taken at the end of cracking (or at intermediate stages if the load was interrupted) the residual strain in the plastic wake can be measured. Following this procedure, contours of the ε_{yy} strain were generated in order to visualize the plastic wake that resulted from the fatigue crack.

Figure 4 compares the plastic wake for fatigue cycling of conventional (Fig. 4a) versus AM-Y3 (Fig. 4b) and AM-Y4 (Fig. 4c) Ti-6Al-4V samples. Note that the white regions within the contours represent uncorrelated points commonly associated with the presence of local voids and of course the crack path, which is clearly illustrated in each case. The crack tip itself was located manually with in situ images taken when fatigue loading was halted. The crack tip location at each load reduction point is indicated by a black dot and the number of cycles and maximum load is called out for each load shedding increment. As aforementioned, load shedding was applied to keep the applied ΔK approximately constant during fatigue crack growth.

The conventional and AM specimens display variability in crack paths, but the plastic wake mostly remains within the width of the machined notch for all samples. The plastic wake that develops in the conventional Ti-6Al-4V (Fig. 4a) is relatively uniform with a symmetric amount of plastic strain developing above and below the crack line for the entire length of the crack. In both AM samples however, the plastic wake is asymmetric about the crack line and varies in

width along the length of the crack. Note that there can be significant variability in the amount of strain accumulated in the wake of the crack in the additive material, as the area of high strain in the plastic wake of the AM-Y3 is larger than in AM-Y4. The reason for this is believed to be a combination of the unique microstructure of the AM material and the voids or defects that may be present. The effect of load shedding is clearly observable in the conventional Ti-6Al-4V sample in Fig. 4a, with the reduction and subsequent growth of the plastic wake corresponding to the points at which the load was reduced. Although occasionally observable, the effect of the load shedding is less clear in the AM samples. Some reductions in plastic wake that correspond to the locations of load shedding are observed in the AM samples, but not for every load shedding point.

The plastic wake contours were also overlaid on the 20x magnification heat tinted optical microstructural images and aligned using the Vickers indents. The resulting plots are shown in Fig. 5. Note that in this set of figures, which contain the same strain data as in Fig. 4, the same contour color levels have been used in all cases so that the relative extent of plasticity between samples can be directly compared. Voids on the order of 30 μm in diameter are observable in the optical microstructural images, as indicated by black arrows in Fig. 5b, and the crack path tends to propagate towards voids. Closer examination of the AM microstructures shows that the plastic wake does stop along the boundary of prior β grains or change direction, as indicated by white arrows in Fig. 5c. Another notable feature is the residual plastic strain that emanates from a void not on the crack path in AM-Y3 in Fig. 5b illustrating the mechanism for voids affecting the approaching fatigue crack line.

3.2 Crack paths

We next examine the influence of microstructure on the fatigue crack path for conventional (Fig. 6) versus AM Ti-6Al-4V (Figs. 7). In constructing these figures, we recorded a 20x grid of images *of the microstructure* in the area of expected crack growth *before* the HiDIC pattern was applied. This allowed for the *eventual* crack path to be digitally overlaid on the *original* microstructure, without the need for additional polishing or material removal. Using ImageJ and Photoshop, the pattern was digitally removed from the 20x magnification images taken after fatigue cracking, leaving only the fatigue crack path. Although an attempt was made to preserve as much of the secondary cracking and crack branching as possible during image processing, often the thin cracks became indistinguishable from the pattern at 20x magnification. An example of the stitched 20x image taken of AM-Y2 after fatigue cracking, but before image processing, is shown in Fig. 7a (upper) for reference. Overlaying the crack path on the heat tinted microstructural images resulted in the remaining images shown in Fig. 7. The images were aligned using the Vickers indentation marks that define the region of interest. The alignment of the crack path and microstructural images had an average error of ±1.5 μm due to a small amount of opening from the crack. This error in alignment meant that the crack path could not be aligned to within a single α' lath. However, the effects of the α' lath direction in the area near the crack could still be observed.

The white arrows in Fig. 7 indicate the regions where crack propagation is parallel to the α' laths, while the red arrows indicate a change in crack path direction that can be attributed to prior β grain boundaries. As shown in the area outlined in red and magnified in Fig. 7a (lower), the main crack stops at a prior β grain boundary and a daughter crack initiates above the main crack, shown by the yellow arrow. The effects of the α' laths and prior β grain boundaries are

also identified for the 1 mm fatigue crack in AM-Y3 and -Y4 in Fig. 7b and 7c, respectively. As noted in Section 3.1, the fatigue crack propagates towards voids on the surface in AM-Y3. The crack paths seen in AM-Y3 and -Y4 exhibit similar behavior to the other AM samples with respect to the α' laths and prior β grain boundaries. This transgranular type of fracture was also observed by Konečná et al. [42] in DMLM Ti-6Al-4V samples. The crack path observed for conventional Ti-6Al-4V, in Fig. 6, is noticeably different than that the AM Ti-6Al-4V samples in Fig. 7. Aside from an initial upward curve in the beginning of the crack, the crack in the conventional material is relatively straight. As seen in the 40x magnification images in Fig. 6, the crack propagates in a transgranular fashion through most observable grains (especially clear in (C)).

The fatigue crack path behavior due to the microstructure of AM Ti-6Al-4V presented here is supported by observations found in several other works. Zhang et al. compared crack propagation and microstructure in WAAM (wire and arc melted) and wrought Ti-6Al-4V [43]. In the wrought Ti-6Al-4V they note that the crack propagates smoothly along the equiaxed grains, while for the WAAM Ti-6Al-4V the crack path is described as torturous due to the lamellar microstructure. Åkerfeldt et al. used EBSD results along the fatigue crack profile to demonstrate that prior β grain boundaries and crystallographic orientations influence the crack profile in laser metal wire deposition (LMWD) Ti-6Al-4V [44]. Sterling et al. attribute the "jaggedness" of the crack propagation path in additive manufactured Ti-6Al-4V to the presence of prior β grains by comparing a Laser Engineered Net Shaping (LENS) Ti-6Al-4V sample with prior β grains to one without [45]. Kumar et al. also note the crack path deflection at prior β grain boundaries in SLM (selective laser melted) Ti-6Al-4V [46].

The tortuosity of the crack path can also be quantified by comparing the horizontal length of each crack to a measurement of the effective, or actual, crack length. These measurements were made in ImageJ, using 4x and 20x magnification images taken of the fatigue crack for each experiment. The results of these measurements for all samples are summarized in Table 1, including an AM-Z1 sample with build orientation along the z-axis that we will discuss in Section 3.4.

Table 1 Comparison of effective and horizontal crack length for conventional and DMLM samples.

Type	Name	Effective Length (mm)	Horizontal Length (mm)	Difference (%)
Conventional	1	2.029	1.975	2.70
	2	1.035	0.997	3.74
AM-Y	1	2.477	2.040	19.4
	2	2.314	1.980	14.0
	3	1.228	0.992	21.3
	4	1.179	1.016	14.9
AM-Z	1	1.390	1.032	29.6

As seen in Table 1, the effective crack length for conventional samples is within 4% of the horizontal crack length, while the effective crack length for the AM-Y samples differs by about

23% from the horizontal length and the AM-Z sample differs by 30%. This tortuosity can result in an increase in required energy to extend the crack [47] which should be an advantage for AM materials in terms of damage tolerance.

3.3 Fracture surfaces

SEM imaging of the entire fracture surfaces was performed for conventional and AM Ti-6Al-4V samples. Figure 8 shows the fracture surface of a conventional sample, where the machined notch, fatigue cracking region, and final fracture region due to monotonic loading (to obtain two pieces) are explicitly labeled as a reference for the remaining fracture surfaces presented in this section. The crack growth direction as defined in Fig. 8, from right to left, applies to all SEM images shown in this section, as all images were taken with the samples in this orientation. As expected, a smooth, thumbnail crack front is seen at the end of the fatigue crack growth region (shown with a dashed red line in Fig. 8). Shear lips that develop during the monotonic loading to failure, and which are consistent with the thin specimens used for testing, are also seen and outlined with dotted white lines in Fig. 8.

SEM images of the fracture surfaces of several AM Ti-6Al-4V samples, subjected to fatigue cracking followed by monotonic loading exceeding 1 kN above the last fatigue cycle load, are shown in Fig. 9. Some voids observable on the fracture surfaces of the AM samples are marked with arrows in Fig. 9 for reference. The fatigue crack fronts seen in the three AM samples (AM-Y1, -Y2, and -Y4) in Fig. 9 are asymmetric and seem to be highly influenced by local three-dimensional effects rather than exhibit the small curvature caused by plane stress to plane strain transition of the conventional Ti-6Al-4V (Fig. 8). Cain et al. also noted an uneven crack front in AM Ti-6Al-4V compact-tension samples used in fracture toughness experiments [15]. As seen in Fig. 9, there is a noticeable increase in the number of pores observed in the monotonic fracture

surface versus the fatigue cracking fracture surface in these AM samples. In comparison to the conventional sample, the shear lips in the AM samples are harder to identify and occupy far less of the sample thickness, perhaps indicating a more brittle fracture or at least indicating a fracture process less controlled by surface plane stress conditions.

The above AM samples exhibited similar global fatigue and fracture response to conventional Ti-6Al-4V. However, we also tested a number of samples (AM-Y3 and AM-Y6) which fractured prematurely when loaded to less than 0.25 kN (versus >1 kN) above the last fatigue cycle maximum load. The fracture surface of AM-Y3, as shown in Fig. 10a, has a similar level of porosity in the fatigue and fracture region compared to the samples shown in Fig. 9. However, a void located close to the surface at the transition from fatigue region to fracture may have been the cause of this premature fracture. This void is shown in a higher magnification image outlined in blue in Fig. 10a.

In addition to these samples, SEM images of the fracture surface were also taken for AM-Y5 sample that unexpectedly failed *during* fatigue cracking. As shown in Fig. 10b, a small amount of fatigue crack propagation is observed for AM-Y5, but transitions to an unstable catastrophic crack when reaching the area where a grouping of voids, outlined in red, is observed in the postmortem SEM image. A higher magnification SEM image of these voids is also shown in Fig. 10b. These spherical voids with smooth inner surfaces are similar to those seen in Sterling et al. [45] for LENS Ti-6Al-4V samples. Sterling et al. also found that an increase in void size, increased number of voids, voids located near the surface, and voids located close together caused a reduction in fatigue life in some cases. Liu and Shin also note that the location and shape of defects in AM Ti-6Al-4V can severely affect the fatigue performance [1]. Williams et

al. cite both a smooth microstructural facet and two partially connected gas pores as the cause for the reduction in cycles to fracture in an EBM (electron beam melted) Ti-6Al-4V sample [48].

Higher magnification images of the fatigue and monotonic fracture regions were taken of the conventional and AM-Y1 Ti-6Al-4V samples, as shown in Fig. 11. The fracture surface of conventional Ti-6Al-4V sample under monotonic loading in Fig. 11a (left) looks as expected, with equiaxed ductile dimples in the monotonic fracture region resulting from a ductile void nucleation, growth, and coalescence failure mechanism. Fatigue striations, perpendicular to the crack propagation direction, are somewhat visible in the fatigue cracking region in Fig. 11a (right). Terracing and shallower dimples in the monotonic fracture region of the AM Ti-6Al-4V in Fig. 11b (left) indicates brittle failure. Wysocki et al. [49] and Mierzejewska et al. [9] attribute this terracing to intergranular fracture, likely along the α' needles. The fatigue cracking region of AM-Y1 shows micro-cracks in different directions, possibly along α' laths. When viewed under even higher magnification (X5,500) fatigue striations can be seen in the fatigue crack propagation region in the conventional sample, as shown in Fig. 12a. At the same magnification, fatigue striations are not easily observed in the AM samples. Instead, at X5,500 magnification micro-cracks are observed in AM-Y2 shown in Fig. 12b.

Voids on the order of ~30 μm are observed on the fracture surface of all AM samples. These voids, that are spherical in nature, are similar to the gas entrapment voids seen in many other studies of AM Ti-6Al-4V [45,50,51] as well as in moisture-encapsulated adhesives [52-54], and can lead to significant reduction in fracture toughness and fatigue cycle life [55]. A higher magnification image of a typical void and un-melted powder particle observed on the fracture surface of AM-Y2 are shown in Fig. 13a and 13b. Some atypical voids that are much larger than

30 μm or elongated, are also observed on the fracture surface of AM-Y2 and -Y6 and are included in Fig. 13c and 13d.

The role of microvoids on the fracture and failure mechanics of conventional metals is well-established. These microvoids nucleate from inclusions and secondary particles at low stress levels during early loading stages, and can have initial void diameters of 2-12 μm [56-59]. Because these void-nucleating particles are uniformly distributed within the metal, the fracture process of void nucleation, growth, and coalescence of conventional metals occurs within a uniformly porous, but narrow, process zone [60-62]. As we have also observed in our fatigue/fracture experiments, these conventional metals exhibit very consistent crack growth behaviors, because the microstructures and precipitate/inclusion distributions do not significantly vary from one conventional metal sample to another. In AM metals, however, there are two separate size-scales of voids. The smaller-scale voids are the same as those present in conventional metals (~2-12 μm) nucleating during loading from inclusions and secondary particles. The larger-scale voids (~30 μm) in AM metals arise from unsintered powder particles or gas entrapment bubbles, as observed on the fracture surfaces of all our AM-Y samples. The distribution of these larger-scale AM voids is also highly stochastic. As shown by our crack growth studies, the surface crack paths can be clearly influenced by the locations of these larger-scale AM voids, thus resulting in at times contradictory fatigue and fracture responses across the AM-Y1 to -Y6 samples which are essentially different instantiations of AM Ti-6Al-4V with the same build direction, manufactured with the same process conditions. Our current surface DIC imaging analysis (Fig. 5) cannot provide detailed 3D information necessary to quantitatively characterize the role of internal voids on fatigue crack propagation (e.g., tunneling effect). Nonetheless, the observed AM voids by SEM represent the fracture surface voids and do give

some indication of their stochastic nature through the thickness that appears to suppress the traditional crack tunneling behavior and rather produce a somewhat tortuous through-thickness crack front as well (dashed lines in Fig. 9).

We have recently performed finite element method (FEM) simulations on crack growth within a process zone containing two-scales of voids representative of AM metals, albeit in two-dimensions [63]. We show that the fracture resistance is significantly impacted by the proportion and size of the larger AM voids within the porous process zone. More importantly, these FEM simulations demonstrate that the crack path is highly sensitive to the location of the AM void with respect to the crack-tip, in agreement with our experiments on the AM-Y specimens, and contribute to the wide scatter in the measured steady-state fracture toughness. A 3D FEM study containing two-size-scale voids is in progress, which could help discern the contribution of internal voids to the fracture and fatigue crack growth response.

3.4 Build orientation effects

To understand the effects of build orientation, we examine the crack path profiles for fatigue cycling of AM-Z1 with build-orientation along the z-axis (i.e., the thickness of the specimen). As shown in Fig. 14a, the prior β grain boundaries and α' laths have similar effects on the crack path regardless of the build orientation (compare Fig. 14a versus Fig. 7). However, the first ~0.25 mm of the crack path in AM-Z1 is distinctly different from all the AM-Y samples: the crack initiates near the center of the notch and grows relatively horizontally, until it deflects at a 90° angle and begins traveling towards a large void on the surface. The influence of the prior β grains on the width and direction of the plastic wake in the AM-Z1 sample can be seen in Fig. 14b. At certain locations, the plastic wake in AM-Z1 is inclined parallel to the prior β grains, and is independent of the crack growth direction. This influence of prior β grains on the plastic wake for AM-Z1

appears to be much stronger than for all of the AM-Y samples with build orientation along the tension direction. Potentially, this is due to the prior β grains of the AM-Z sample which are oriented at ~45° to the desired crack propagation path, versus those in the AM-Y samples which are oriented perpendicular to the desired crack propagation path.

Figure 15a shows the fracture surface of the AM-Z1 sample, with dashed red lines separating the fatigue cracking region (right) from the fracture (left) region associated with monotonic loading. Compared to the AM-Y samples in Figs. 10 and 11, the AM-Z1 sample has noticeably fewer voids on the fracture surface and has a relatively straight crack front. However, the AM-Z1 sample still failed prematurely when loaded to <0.25 kN above the last fatigue cycle maximum load. The underpinning reason for this remains unclear, since higher magnification imaging in Fig. 15b shows similar micro-cracking along the α' laths in the fatigue region as well as terracing and shallower dimples in the monotonic fracture region to the AM-Y samples. One possible explanation could rest with residual stresses which are expected to be very different in the two builds (Z vs. Y) because of differing thermal histories in the samples.

4. Conclusions

The main goal of this work was to compare the microstructures of AM versus conventionally manufactured Ti-6Al-4V alloys and to determine how the microstructural differences impact strain accumulation and crack path during fatigue cycling. In pursuit of this goal, high-resolution ex situ HiDIC-measured strain fields were overlaid on optical microstructural images of heat tinted samples. The differences in microstructures between the AM and conventionally manufactured Ti-6Al-4V resulted in noticeable differences in the size and behavior of the plastic wake that developed from fatigue cracking. The plastic wake in the conventional sample was

symmetric and responded predictably to load shedding, while the plastic wake in the additive samples was asymmetric and unpredictable, meaning that it sometimes responded to the reduction of load and sometimes not. The overlay of the fatigue crack path on the microstructural images further supported the observations that the microstructure influences fatigue crack propagation. Regions where the crack propagated along α' laths and deflected at prior β grain boundaries were observed in all AM samples, regardless of build orientation. The fatigue crack also propagated towards voids on the surface which implied that defects, such as voids, play a significant role in the fatigue and fracture behavior of the AM samples. The premature failure of several AM samples during fatigue cracking, or subsequent monotonic loading, could also be attributed to the defects in the AM samples, which suggests that controlling these AM void defects is key to improving reliability of these materials.

Acknowledgements

HBC acknowledges the support of the National Science Foundation Grant No. NSF-DMR-18-09696 and AFOSR award FA9550-19-1-0242, and JL acknowledges the support of the DOE NEUP award number DE-NE0008436 and AFOSR award FA9550-16-1-0055. RV is also grateful to the University of Illinois Aerospace Engineering Department for a Stillwell fellowship award. We also gratefully acknowledge Ms. Audrey Lee for her assistance with the preparation of samples used in this work. This research was carried out in part in the Advanced Materials Testing and Evaluation Laboratory, and in the Materials Research Laboratory Central Research Facilities, University of Illinois.

Data availability statement

The raw/processed data required to reproduce these findings cannot be shared at this time as the data also forms part of an ongoing study.

References

[1] S. Liu and Y. C. Shin, "Additive manufacturing of Ti6Al4V alloy: A review," Materials & Design, vol. 164, p. 107552, 2019.

[2] M. K. Thompson, G. Moroni, T. Vaneker, G. Fadel, R. I. Campbell, I. Gibson, A. Bernard, J. Schulz, P. Graf, B. Ahuja and F. Martina, "Design for Additive Manufacturing: Trends, opportunities, considerations, and constraints," CIRP Annals, vol. 65, no. 2, pp. 737-760, 2016.

[3] R. G. Clinton, "NASA's In Space Manufacturing Initiative and Additive Manufacturing Development and Quality Standards Approach for Rocket Engine Space Flight Hardware," in Additive Manufacturing for Defense and Aerospace 2016 Summit, London, 2016.

[4] S. H. Khajavi, J. Partanen and J. Holmström, "Additive manufacturing in the spare parts supply chain," Computers in Industry, vol. 65, no. 1, pp. 50-63, 2014.

[5] B. Dutta and F. H. Froes, Additive Manufacturing of Titanium Alloys, Cambridge: Elsevier, 2016.

[6] G. Lütjering and J. C. Williams, Titanium, New York: Springer, 2003.

[7] M. Neikter, P. Åkerfeldt, R. Pederson, M.-L. Antti and V. Sandell, "Microstructural characterization and comparison of Ti-6Al-4V manufactured with different additive manufacturing processes," Materials Characterization, vol. 143, pp. 68-75, 2018.

[8] R. Mulay, J. Moore, J. Florando, N. Barton and M. Kumar, "Microstructure and mechanical properties of Ti–6Al–4V: Mill-annealed versus direct metal laser melted alloys," Materials Science & Engineering A, vol. 666, pp. 43-47, 2016.

[9] Z. A. Mierzejewska, R. Hudák and J. Sidun, "Mechanical Properties and Microstructure of DMLS Ti6Al4V Alloy Dedicated to Biomedical Applications," Materials, vol. 12, p. 176, 2019.

[10] X. Wu, J. Liang, J. Mei, C. Mitchell, P. Goodwin and W. Voice, "Microstructures of laser-deposited Ti–6Al–4V," Materials & Design, vol. 25, pp. 137-144, 2004.

[11] Y. Han, W. Lu, T. Jarvis, J. Shurvinton and X. Wu, "Investigation on the Microstructure of Direct Laser Additive Manufactured Ti6Al4V Alloy," Materials Research, vol. 18, pp. 24-28, 2015.

[12] J. Lin, Y. Lv, Y. Liu, B. Xu, Z. Sun, Z. Li and Y. Wu, "Microstructural evolution and mechanical properties of Ti-6Al-4V wall deposited by pulsed plasma arc additive manufacturing," Materials and Design, vol. 102, pp. 30-40, 2016.
[13] T. H. Becker, M. Beck and C. Scheffer, "Microstructure and Mechanical Properties of Direct Metal Laser Sintered Ti-6Al-4V," South African Journal of Industrial Engineering, vol. 26, no. 1, pp. 1-10, 2015.
[14] B. Van Hooreweder, D. Moens, R. Boonen, J. Kruth and P. Sas, "Analysis of Fracture Toughness and Crack Propagation of Ti6Al4V Produced by Selective Laser Melting," Advanced Engineering Materials, vol. 14, no. 1-2, pp. 92-97, 2011.
[15] V. Cain, L. Thijs, J. Van Humbeeck, B. Van Hooreweder and R. Knutsen, "Crack propagation and fracture toughness of Ti6Al4V alloy produced by selective laser melting," Additive Manufacturing, vol. 5, pp. 68-76, 2015.
[16] D. Greitemeier, F. Palm, F. Syassen and T. Melz, "Fatigue performance of additive manufactured TiAl6V4 using electron and laser beam melting," International Journal of Fatigue, vol. 94, pp. 211-217, 2017.
[17] P. Edwards and M. Ramulu, "Effect of build direction on the fracture toughness and fatigue crackgrowth in selective laser melted Ti-6Al-4V," Fatigue & Fracture of Engineering Materials & Structures, vol. 38, no. 10, pp. 1228-1236, 2015.
[18] G. Nicoletto, "Anisotropic high cycle fatigue behavior of Ti–6Al–4V obtained by powder bed laser fusion," International Journal of Fatigue, vol. 94, pp. 255-262, 2017.
[19] T. M. Mower and M. J. Long, "Mechanical behavior of additive manufactured, powder-bed laser-fused materials," Materials Science and Engineering: A, vol. 651, pp. 198-213, 2016.
[20] M. Simonelli, "Microstructure evolution and mechanical properties of selective laser melted Ti-6Al-4V," Doctoral Thesis, Department of Materials, Loughborough University, Loughborough, 2014.
[21] J. Carroll, J. Abuzaid, J. Lambros and H. Sehitoglu, "An experimental methodology to relate local strain to microstructural texture," Review of Scientific Instruments, vol. 81, p. 083703, 2010.
[22] K. Wang, F. Wang, W. Cui, T. Hayat and B. Ahmad, "Prediction of short fatigue crack growth of Ti-6Al-4V," Fatigue & Fracture of Engineering Materials & Structures, vol. 37, no. 10, pp. 1075-1086, 2014.
[23] S. Preibisch, S. Saalfeld and P. Tomancak, "Globally optimal stitching of tiled 3D microscopic image acquisitions," Bioinformatics, vol. 25, no. 11, pp. 1463-1465, 2009.
[24] G. F. Vander Voort, Metallography Principles and Practice, Materials Park, OH: ASM International, 1999.
[25] M. L. Harper, Y. Kosaka and S. P. Fox, "Titanium Metallography Using Heat Tinting," in Ti-2007: Science and Technology; Proceedings of the 11th World Conference on Titanium (JIMIC5), Kyoto, 2007.
[26] D. Barnes, "Heat Tinting of Titanium and Titanium Alloys," Metallography, Microstructure, and Analysis, vol. 5, no. 6, pp. 536-539, 2016.
[27] H. Rafi, N. Karthik, H. Gong, T. L. Starr and B. E. Stucker, "Microstructures and Mechanical Properties of Ti6Al4V Parts Fabricated by Selective Laser Melting and

Electron Beam Melting," Journal of Materials Engineering and Performance, vol. 22, no. 12, pp. 3872-3883, 2013.
[28] A. Gupta, R. K. Khatirkar, A. Kumar and M. S. Parihar, "Investigations on the effect of heating temperature and cooling rate on evolution of microstructure in an α + β titanium alloy," Journal of Materials Research, vol. 33, no. 8, pp. 946-957, 2018.
[29] B. Sefer, Oxidation and Alpha–Case Phenomena in Titanium Alloys used in Aerospace Industry: Ti–6Al–2Sn–4Zr–2Mo and Ti–6Al–4V, Luleå, Sweden: Luleå University of Technology, Department of Engineering Sciences and Mathematics, Licentiate Thesis, 2014.
[30] J.-T. Yeom, J. H. Kim, J.-K. Hong, N.-K. Park and C. S. Lee, "Prediction of Microstructure Evolution in Hot Backward Extrusion of Ti-6Al-4V Alloy," Journal of Metallurgy, vol. 2012, pp. 1-6, 2011.
[31] A. Z. Mierzejewska, R. Hudák and J. Sidun, "Mechanical Properties and Microstructure of DMLS Ti6Al4V Alloy Dedicated to Biomedical Applications," Materials, vol. 12, no. 1, pp. 176, 2019.
[32] Y. Xu, Y. Lu, J. Liang and R. D. Sisson, "Microstructure and corrosion behavior of additively manufactured Ti–6Al–4V with various post-heat treatments," Materials Science and Technology, vol. 35, no. 1, pp. 89-97, 2019.
[33] J. Brezinová, R. Hudák, A. Guzanová, D. Draganovská, G. Ižaríková and J. Koncz, "Direct Metal Laser Sintering of Ti6Al4V for Biomedical Applications: Microstructure, Corrosion Properties, and Mechanical Treatment of Implants," Metals, vol. 6, pp. 171, 2016.
[34] P. Kobryn and S. Semiatin, “The Laser Additive Manufacture of Ti-6Al-4V,” JOM, vol. 53, pp. 40-42, 2001.
[35] P. Kobryn and S. Semiatin, “Microstructure and Texture Evolution During Solidification Processing of Ti-6Al-4V,” Journal of Materials Processing Technology, vol. 135, pp. 330-339, 2003.
[36] S. Kelly and S. Kampe, “Microstructural Evolution in Laser-Deposited Multilayer Ti-6Al-4V Builds: Part I,” Microstructural Characterization,” Metallurgical and Materials Transactions A, vol. 35, pp.1861-1867, 2004.
[37] B. Baufield, O. Van der Biest and R. Gault, “Additive Manufacturing of Ti-6Al-4V Components by Shaped Metal Deposition: Microstructure and Mechanical Properties,” Materials and Design,vol. 31, pp. S106-S111, 2010.
[38] L. Thijs, F. Verhaeghe, T. Craeghs, J. Van Humbeeck and J.-P. Kruth, “A Study of the Microstructural Evolution During Selective Laser Melting of Ti-6Al-4V. Acta Materiala, vol. 58, pp. 3303-3312, 2010.
[39] L. Murr, S. Quinones, S. Gaytan, M. Lopez, A. Rodela, E.Y. Martinez,D.H. Hernandez, E. Martinez, F. Medina, R.B. Wicker, “Microstructure and Mechanical Behavior of Ti-6Al-4V Produced by Rapid-Layer Manufacturing, for Biomedical Applications,” Journal of the Mechanical Behavior of Biomedical Materials, Vol. 2, pp. 20-32, 2009.
[40] Y. Zhai, D.A. Lados, E.J, Brown and G.N. Vigilante, G. N., “Fatigue Crack Growth Behavior and Microstructural Mechanisms in Ti-6Al-4V Manufactured by Laser Engineered Net Shaping,” International Journal of Fatigue, vol. 93, pp. 51-63, 2016.

[41] B.E. Carroll, T.A. Palmer and A.M. Beese, “Anisotropic Tensile Behavior of Ti-6Al-4V Components Fabricated with Directed Energy Deposition Additive Manufacturing,” Acta Materiala, vol. 87, pp. 309-320, 2015.
[42] R. Konečná, L. Kunz, A. Bača and G. Nicoletto, "Long fatigue crack growth in Ti6Al4V produced by direct metal laser sintering," Procedia Engineering, vol. 160, pp. 69-76, 2016.
[43] J. Zhang, X. Zhang, X. Wang, Y. Traoré, S. Paddea and S. Williams, "Crack path selection at the interface of wrought and wire arc additive manufactured Ti–6Al–4V," Materials & Design, vol. 104, pp. 365-375, 2016.
[44] P. Åkerfeldt, M. H. Colliander, R. Pederson and M.-L. Antti, "Electron backscatter diffraction characterization of fatigue crack growth in laser metal wire deposited Ti-6Al-4V," Materials Characterization, vol. 135, pp. 245-256, 2018.
[45] A. Sterling, N. Shamsaei, B. Torries and S. M. Thompson, "Fatigue Behavior of Additively Manufactured Ti-6Al-4V," Procedia Engineering, vol. 133, pp. 576-589, 2015.
[46] P. Kumar, O. Prakash and U. Ramamurty, "Micro-and meso-structures and their influence on mechanical properties of selectively laser melted Ti-6Al-4V," Acta Materialia, vol. 154, pp. 246-260, 2018.
[47] H. Galarraga, R. J. Warren, D. A. Lados, R. R. Dehoff and M. M. Kirka, "Fatigue crack growth mechanisms at the microstructure scale in as-fabricated and heat treated Ti-6Al-4V ELI manufactured by electron beam melting (EBM)," Engineering Fracture Mechanics, vol. 176, pp. 263-280, 2017.
[48] S. Tammas-Williams, P. Withers, I. Todd and P. Prangnell, "The Influence of Porosity on Fatigue Crack Initiation in Additively Manufactured Titanium Components," Scientific Reports, vol. 7, p. 7308, 2017.
[49] B. Wysocki, P. Maj, R. Sitek, J. Buhagiar , K. J. Kurzydłowski and W. Swieszkowski, "Laser and Electron Beam Additive Manufacturing Methods of Fabricating Titanium Bone Implants," Applied Sciences, vol. 7, p. 657, 2017.
[50] H. Galarraga, D. A. Lados, R. R. Dehoff, M. M. Kirka and P. Nandwana, "Effects of the microstructure and porosity on properties of Ti-6Al-4V ELI alloy fabricated by electron beam melting (EBM)," Additive Manufacturing, vol. 10, pp. 47-57, 2016.
[51] P. Edwards, A. O'Connor and M. Ramulu, "Electron Beam Additive Manufacturing of Titanium Components: Properties and Performance," Journal of Manufacturing Science and Engineering, vol. 135, p. 061016, 2013.
[52] H.B. Chew, T.F. Guo and L. Cheng, “Vapor pressure and residual stress effects on the toughness of polymeric adhesive joints,” Engineering Fracture Mechanics, vol. 71, pp. 2435-2448, 2004.
[53] H.B. Chew, T.F. Guo and L. Cheng, “Vapor pressure and residual stress effects on mixed mode toughness of an adhesive film,” International Journal of Fracture, vol. 134, pp. 349-368, 2005.
[54] H.B. Chew, S. Hong and K.-S. Kim, “Cohesive zone laws for void growth – II. Numerical field projection of elasto-plastic fracture processes with vapor pressure,” Journal of the Mechanics and Physics of Solids, vol. 57, pp. 1374-1390, 2009.

[55] H.B. Chew, “Cohesive zone laws for fatigue crack growth: Numerical field projection of the micromechanical damage process in an elaso-plastic medium,” International Journal of Solids and Structures, vol. 51, pp. 1410-1420, 2014.
[56] R.H. Van Stone, T.B. Cox, J.R. Low Jr. and J.A. Psioda, “Microstructural aspects of fracture by dimpled rupture,” Int. Met. Rev., vol. 30, pp. 157-179, 1985.
[57] J. Faleskog and C.F. Shih, “Micromechanics of coalescence – I. Synergistic effects of elasticity, plastic yielding and multi-size scale voids,” J. Mech. Phys. Solids, vol. 45, pp. 21-50, 1997.
[58] H.B. Chew, T.F. Guo and L. Cheng, L., “Effects of pressure-sensitivity and plastic dilatancy on void growth and interaction,” Int. J. Solids Struct., vol. 43, pp. 6380-6397, 2006.
[59] V. Tvergaard, “Interaction of very small voids with larger voids,” Int. J. Solids Struct., vol. 35, pp. 3989-4000, 1998.
[60] H.B. Chew, T.F. Guo and L. Cheng, L., “Vapor pressure and residual stress effects on failure of an adhesive film,” Int. J. Solids Struct., Vol. 42, pp. 4795-4810, 2005.
[61] H.B. Chew, T.F. Guo and L. Cheng, “Pressure-sensitive ductile layers–I. Modeling the growth of extensive damage,” Int. J. Solids Struct., vol. 44, pp. 2553-2570, 2007.
[62] H.B. Chew, T.F. Guo and L. Cheng, “Pressure-sensitive ductile layers–II. 3D models of extensive damage,” Int. J. Solids Struct., vol. 44, pp. 5349-5368, 2007.
[63] Y. Cui, Y.F. Gao and H.B. Chew, “Two-scale porosity effects on cohesive crack growth in a ductile media,” Int. J. Solids Struct., vol. 200-201, pp. 188-197, 2020.

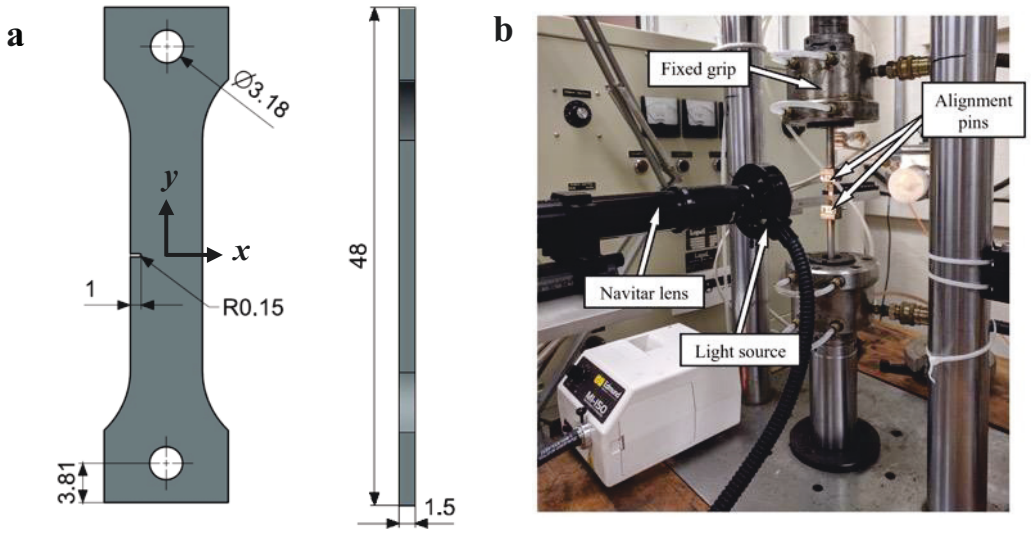

Figure 1: (**a**) Schematic of additively manufactured Ti-6Al-4V samples (all dimensions in mm). (**b**) In situ DIC tension test set up on Instron 8500 machine.

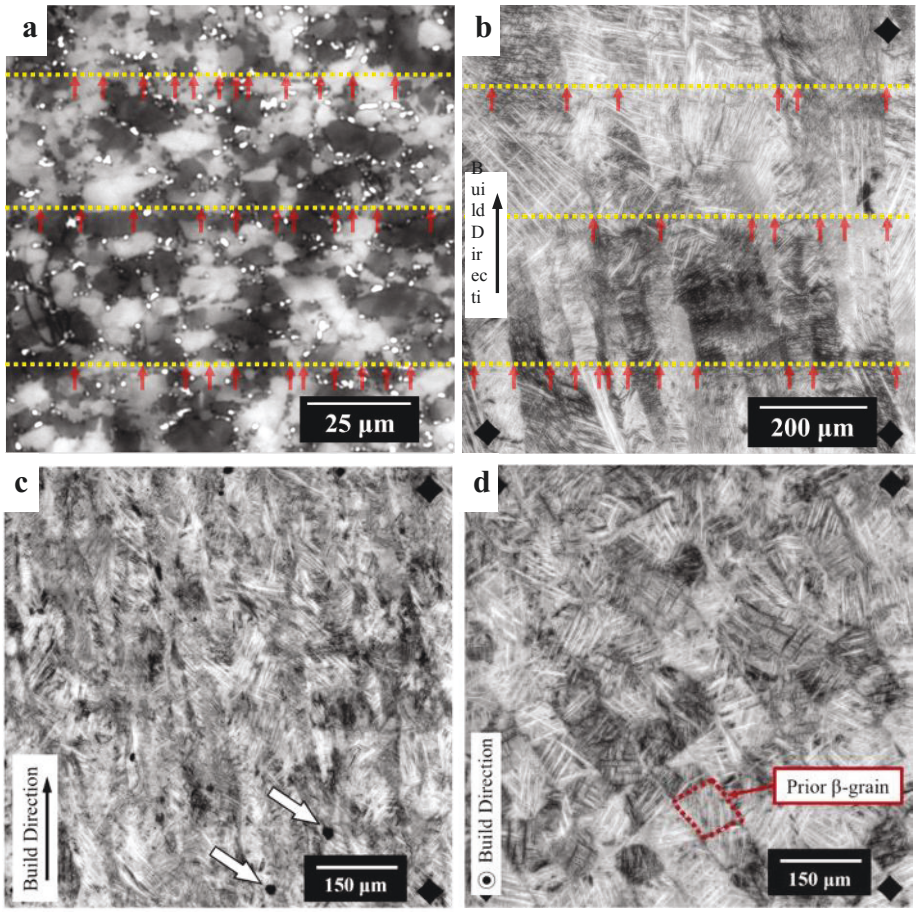

Figure 2: Heat tinted microstructures of conventional (**a**) versus three AM-produced Ti-6Al-4V samples termed AM-Y4 (**b**), AM-Y3 (**c**), and AM-Z1 (**d**). Red arrows in (**a,b**) indicate observed grain boundaries along yellow dashed lines. White arrows in (**c**) indicate examples of voiding defects from AM processing.

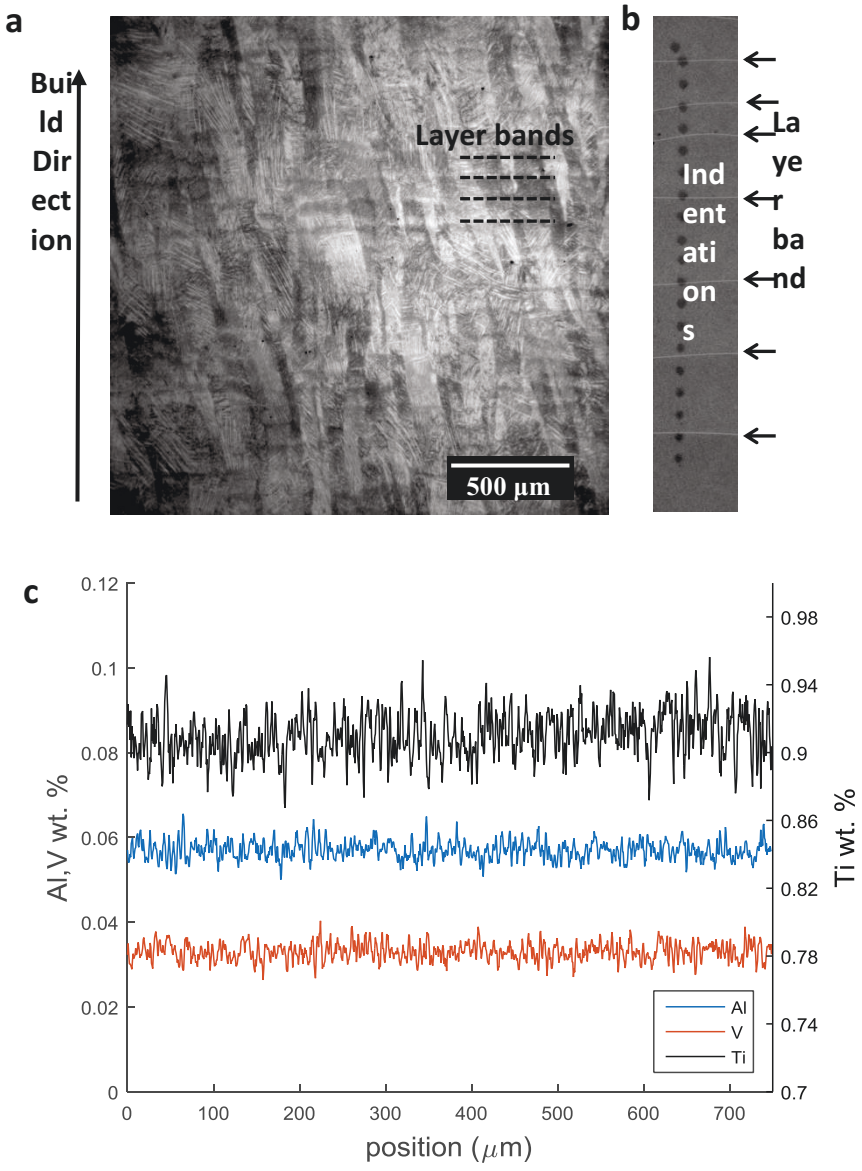

Figure 3: (**a**) Layering bands in the AM-Y1 sample. (**b**) Close-up view of the microhardness indentations superposed on an SEM image, with lines indicating locations of layering bands. (**c**) Energy dispersive electron spectroscopy line scan showing the composition changes of the various constituent elements along the build direction.

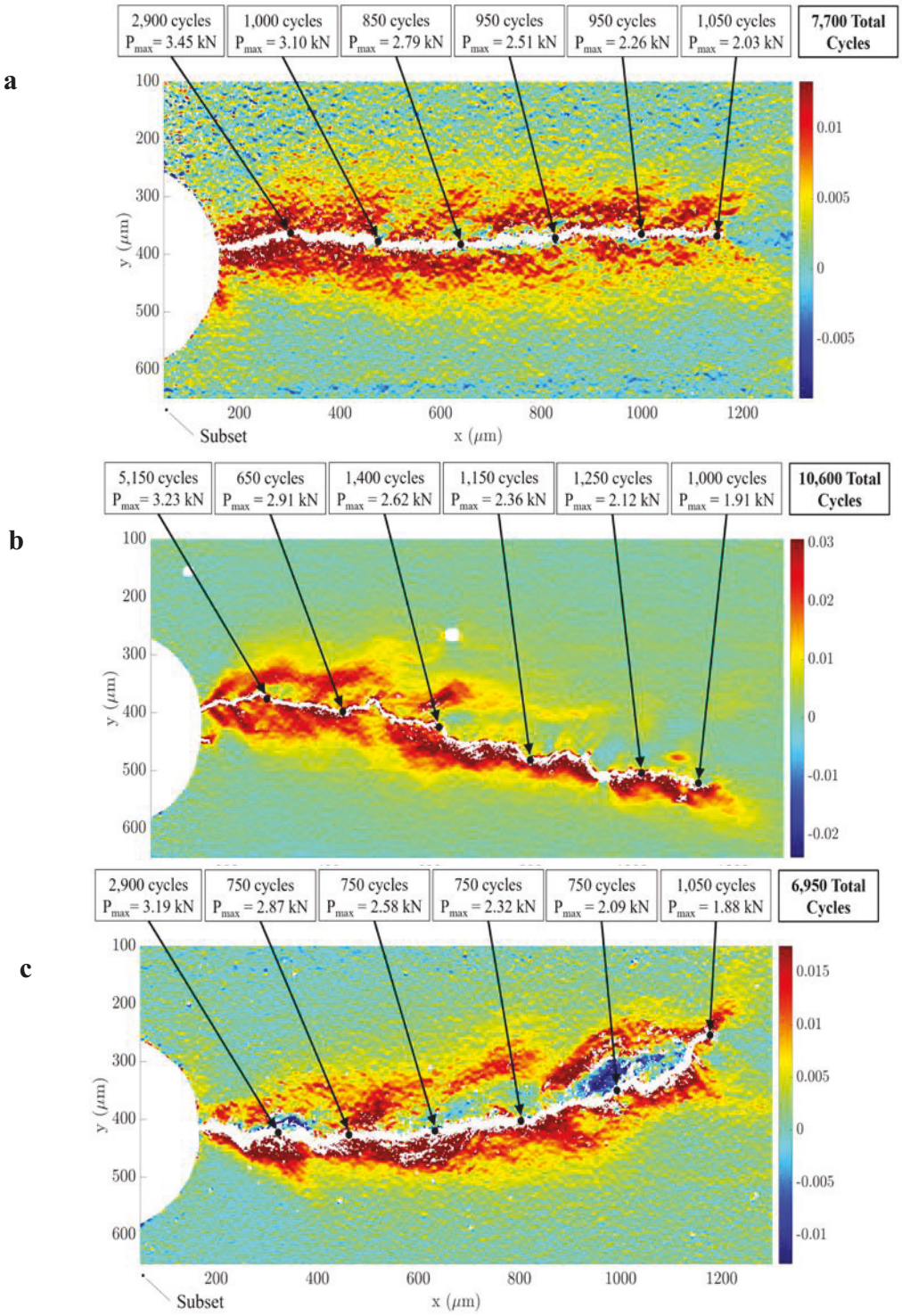

Figure 4: Plastic wake for fatigue cycling of conventional (**a**), AM-Y3 (**b**), and AM-Y4 (**c**) Ti-6Al-4V samples, each with a 1 mm fatigue crack. Arrows denote the location of each load shedding point, with associated number of cycle increments and maximum load as marked.

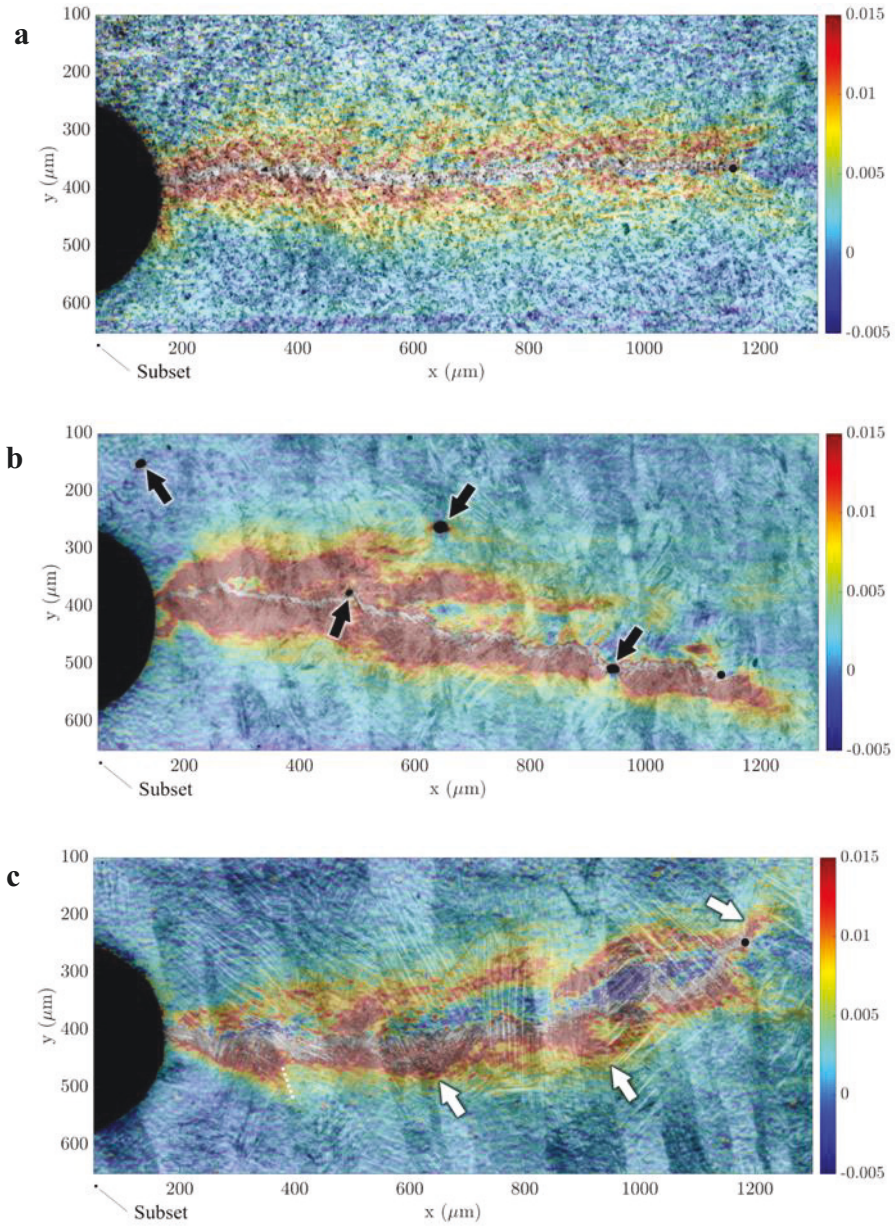

Figure 5: Plastic wake overlaid on heat tinted microstructural images for fatigue cycling of conventional (**a**), AM-Y3 (**b**), and AM-Y4 (**c**) Ti-6Al-4V samples, each with a 1mm fatigue crack.

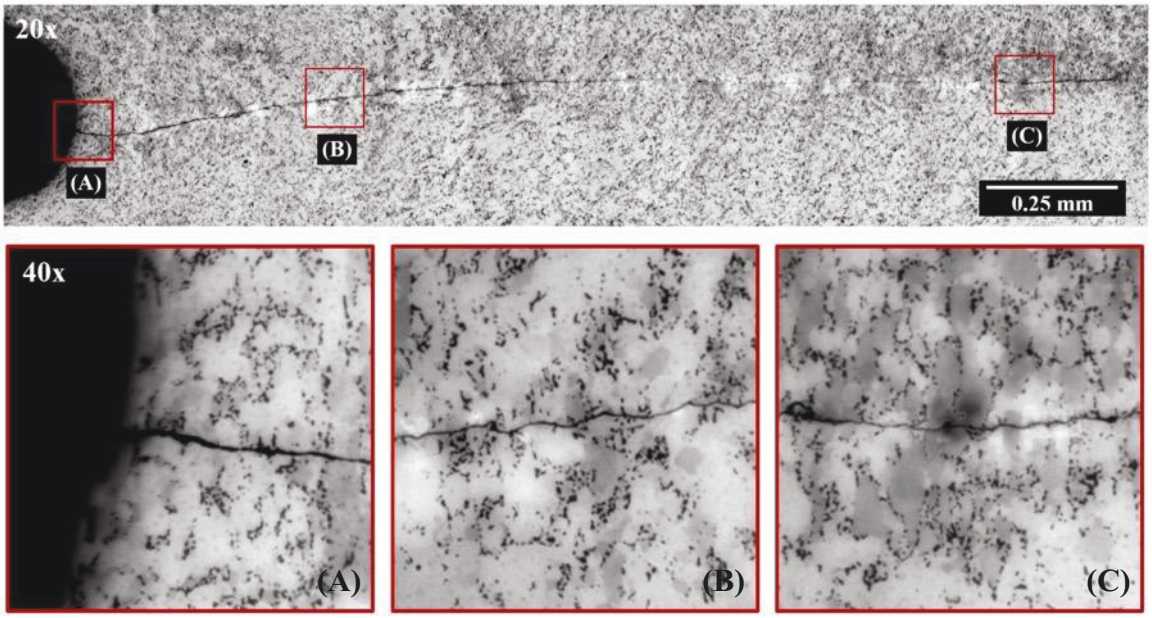

Figure 6: Crack path profile of conventional Ti-6Al-4V with close up view (**A**) to (**C**) of three regions of interest.

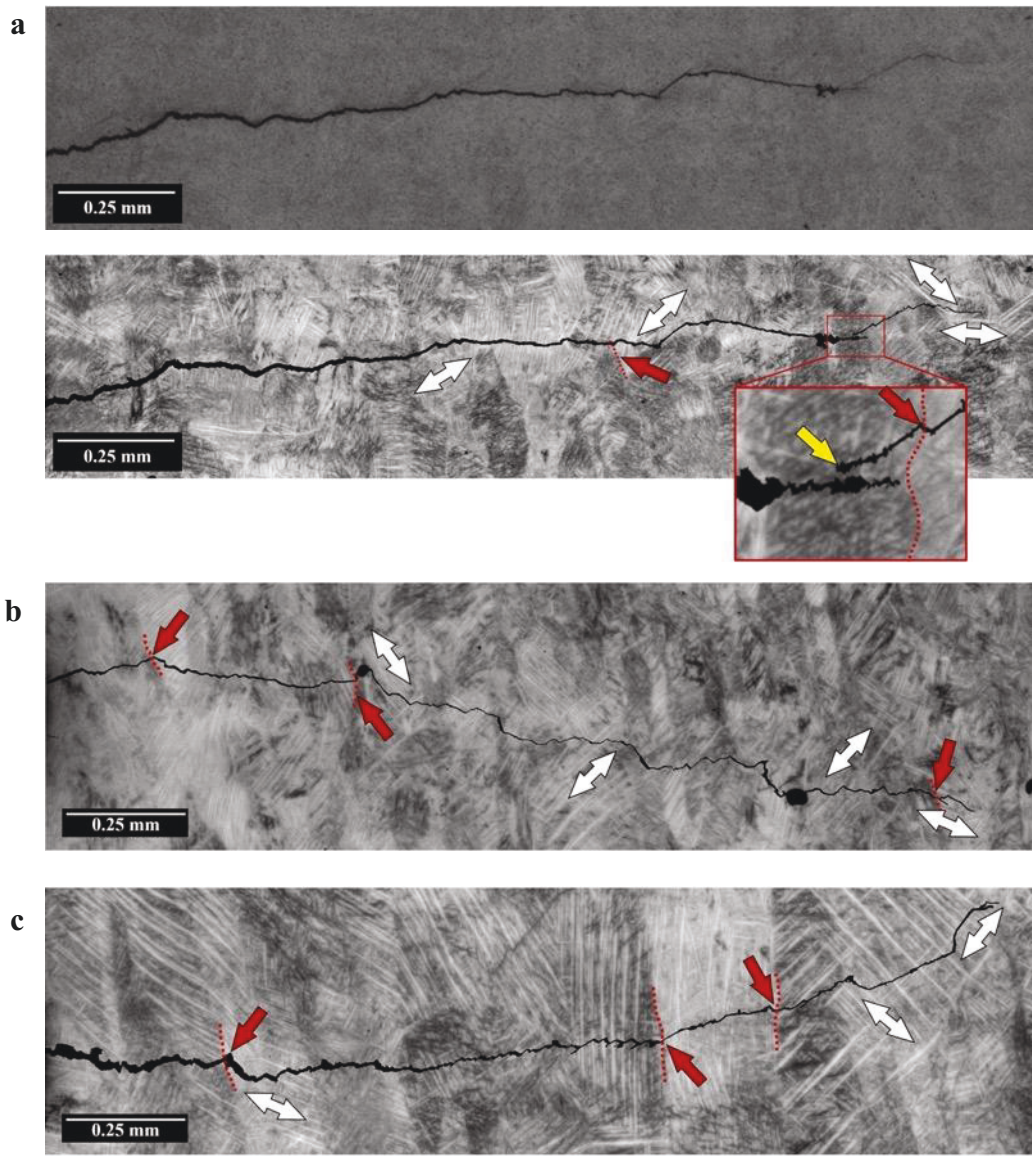

Figure 7: Crack path profiles of AM-Y2 (**a**) AM-Y3 (**b**), and AM-Y4 (**c**) Ti-6Al-4V samples. Upper and lower images in (**a**) are the crack path profiles before image processing and overlaid on microstructure. White and red arrows indicate the effects of α' laths and prior β grain boundaries on crack path, respectively; yellow arrow indicates the formation of a daughter crack.

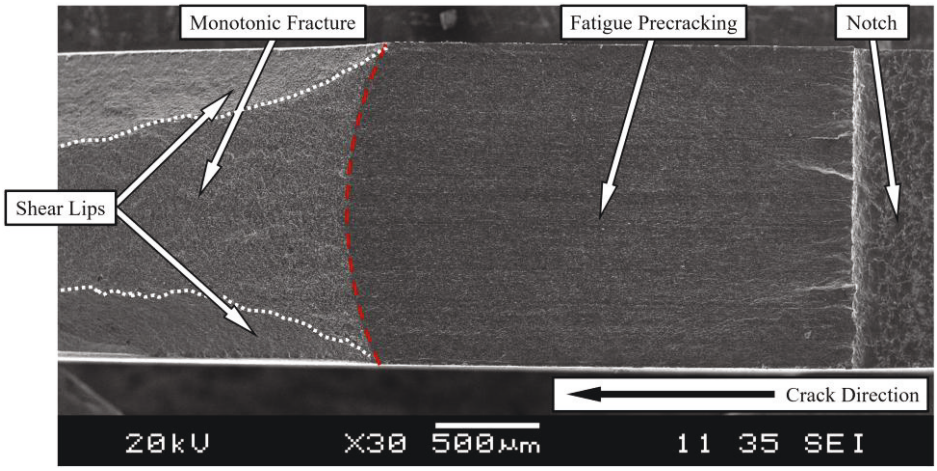

Figure 8: SEM image of the fracture surface of a typical conventional Ti-6Al-4V sample. Red dashed lines outline the final location of the fatigue crack front before final fracture under monotonic loading. White dotted lines indicate shear lips that develop during monotonic fracture.

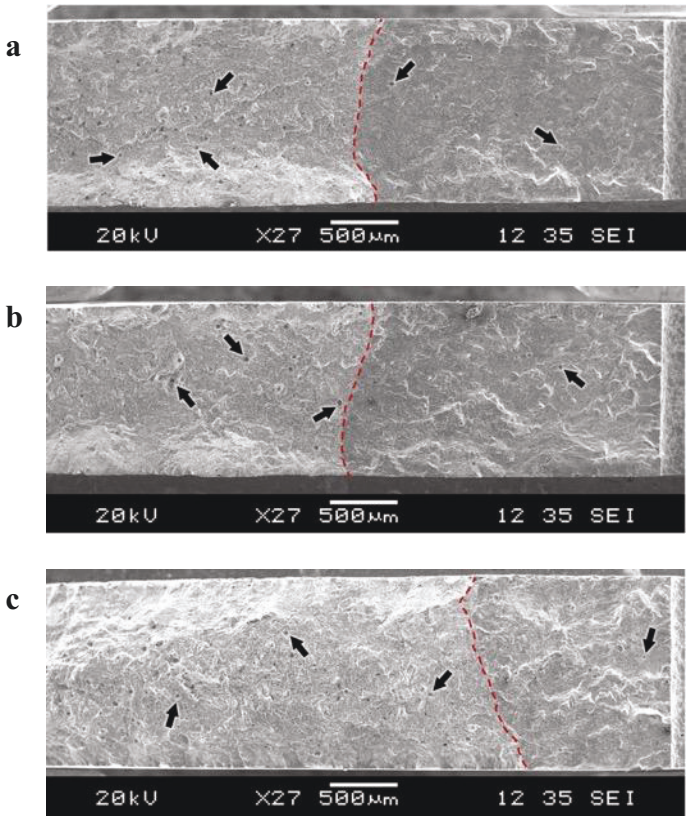

Figure 9: SEM image of the fracture surfaces of AM-Y1 (**a**), AM-Y2 (**b**), and AM-Y4 (**c**) Ti-6Al-4V samples subjected to monotonic loading at loads > 1kN following fatigue cracking. Red dashed lines outline the fatigue crack front denoting the transition from fatigue to fracture. Black arrows indicate some of the observable voids on the fracture surface.

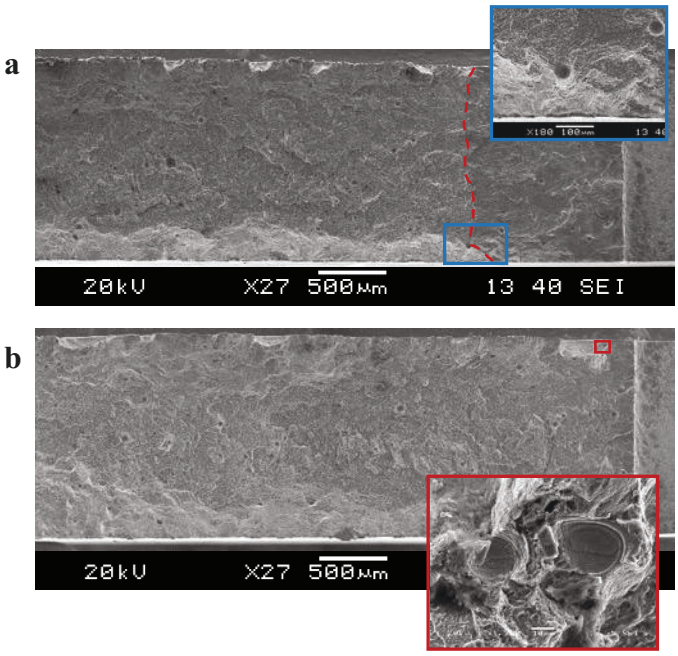

Figure 10: SEM image of the fracture surface of AM-Y3 (**a**) and AM-Y5 (**b**) Ti-6Al-4V samples. Sample (**a**) failed prematurely when loaded to <0.25 kN above the last fatigue cycle maximum load, while sample (**b**) failed prematurely at a load below the maximum load of its last fatigue cycle. Close-up views in (**a**) and (**b**) respectively show voids along the fatigue crack front and clustering of voids, which are responsible for the premature failure. Red dashed line in (**a**) outlines the fatigue crack front denoting the transition from fatigue to fracture.

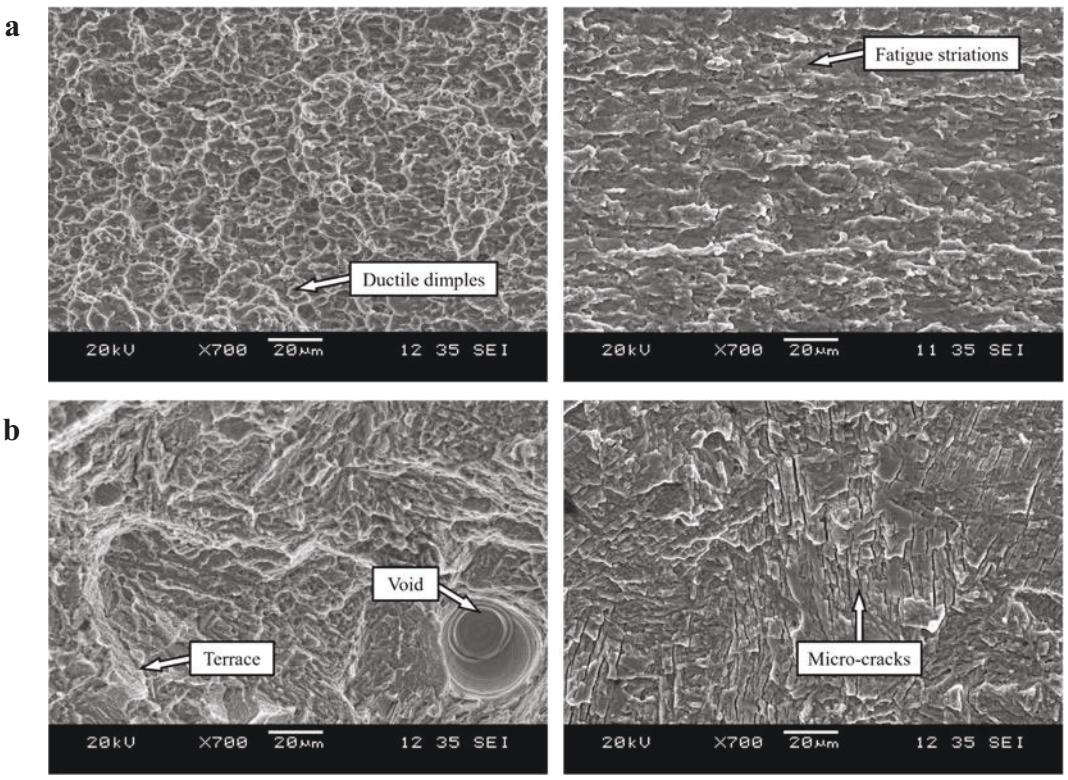

Figure 11: SEM images of the fracture (left) and fatigue (right) surfaces of conventional (**a**) and AM-Y1 (**b**) Ti-6Al-4V samples.

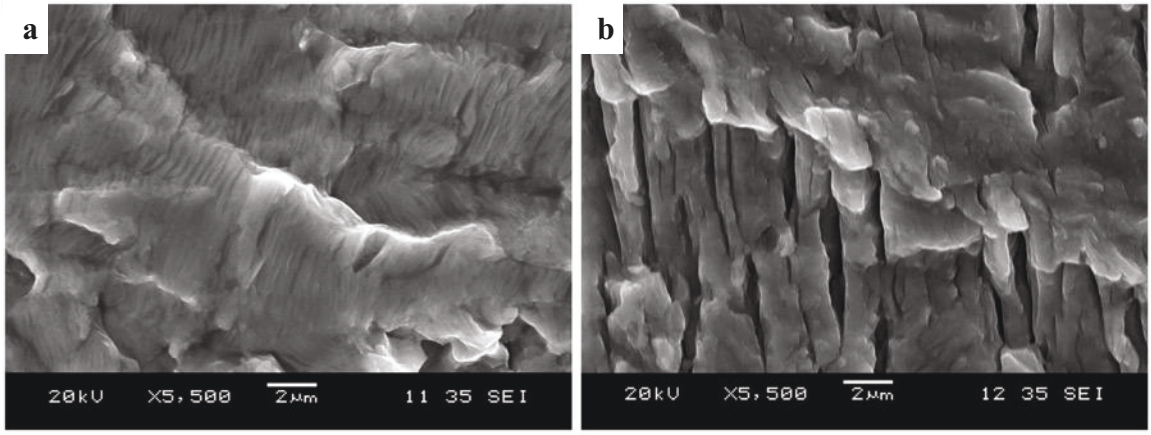

Figure 12: High magnification SEM images of fatigue striations (**a**) and microcracking (**b**) in the fatigue regions of conventional and AM-Y2 Ti-6Al-4V samples, respectively.

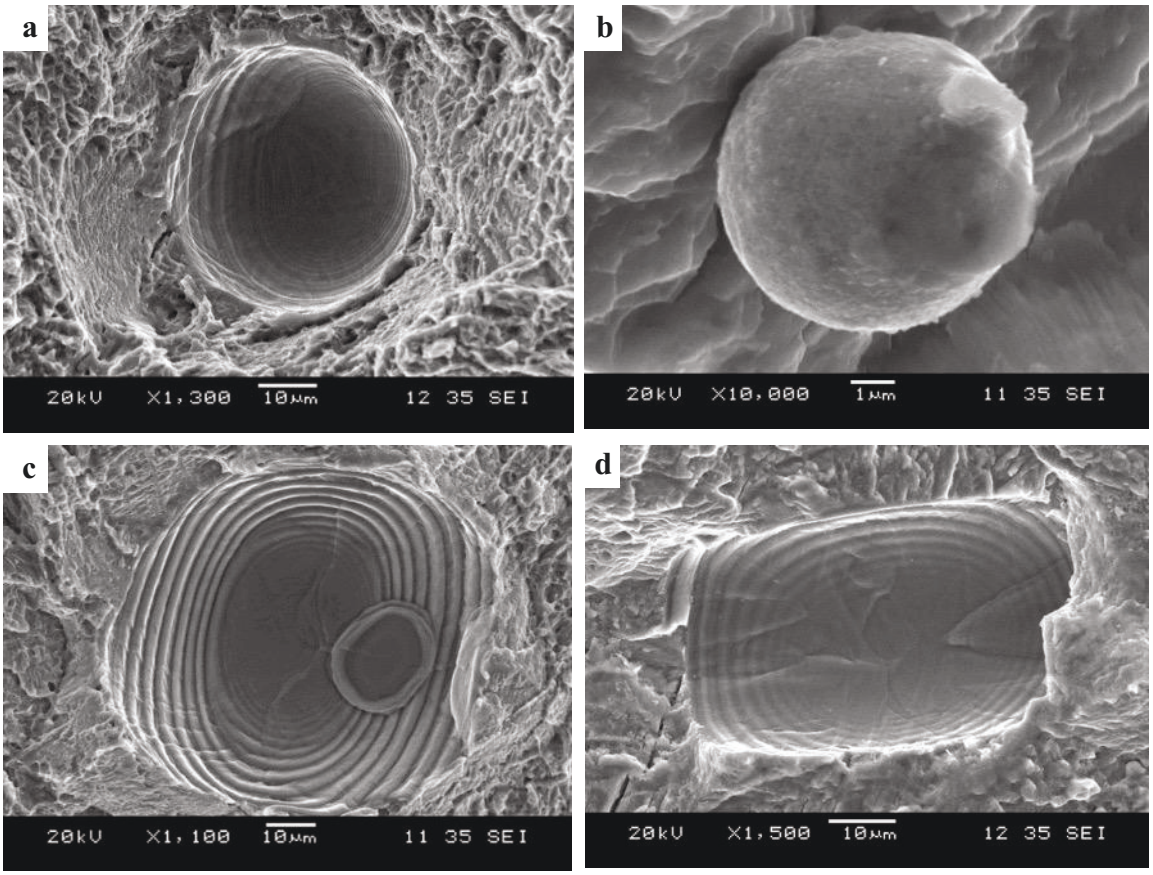

Figure 13: High magnification SEM images of void-like defect (**a**) and unsintered powder particle (**b**) on the fracture surfaces of AM-Y2 Ti-6Al-4V sample, as well as atypical voids found on AM-Y6 (**c**) and AM-Y2 (**d**) Ti-6Al-4V samples.

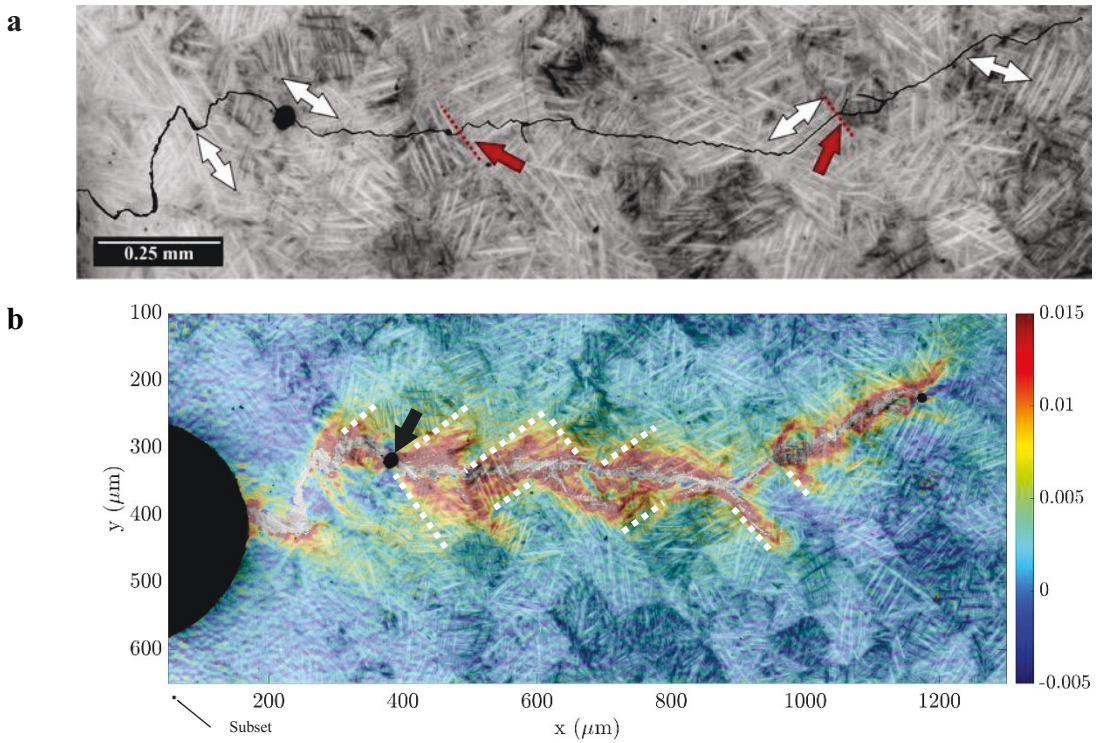

Figure 14: (**a**) Crack path profiles for fatigue cycling of AM-Z1 Ti-6Al-4V sample. White arrows indicate the effects of the α′ laths and red arrows indicate effects of prior β grain boundaries on crack path. (**b**) Plastic wake overlaid on heat tinted microstructural image in (**a**). Voids are denoted by black arrows. Observable effects of prior β grains on the plastic wake are denoted by white dashed lines.

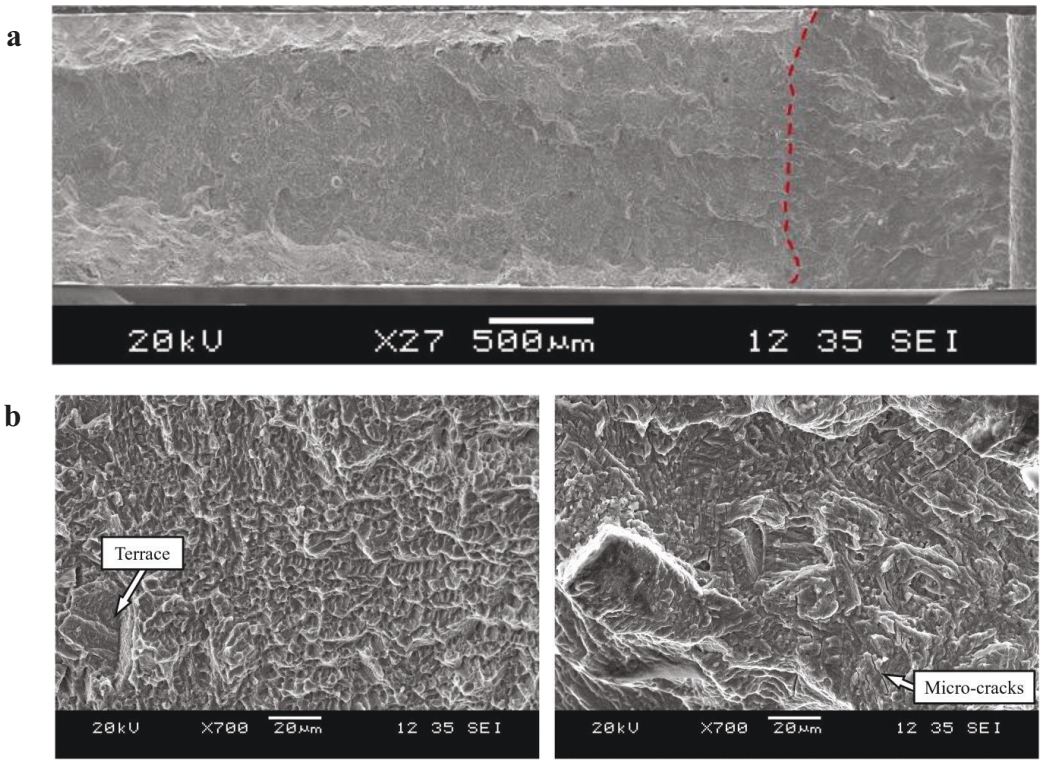

Figure 15: (**a**) SEM image of the fracture surface of AM-Z1 Ti-6Al-4V sample, which failed prematurely when loaded to <0.25 kN above the last fatigue cycle maximum load. (**b**) High magnification SEM images of the fracture (left) and fatigue regions (right) of AM-Z1 sample.